ARMAR: An Airborne Rain-Mapping Radar

S. L. DURDEN, E. IM, F. K. LI, W. RICKETTS, A. TANNER, AND W. WILSON

Jet Propulsion Laboratory, California Institute of Technology, Pasadena, California

(Manuscript received 26 April 1993, in final form 6 October 1993)

ABSTRACT

A new airborne rain-mapping radar (ARMAR) has been developed by NASA and the Jet Propulsion Laboratory for operation on the NASA Ames DC-8 aircraft. The radar operates at 13.8 GHz, the frequency to be used by the radar on the Tropical Rainfall Measuring Mission (TRMM). ARMAR simulates the TRMM radar geometry by looking downward and scanning its antenna in the cross-track direction. This basic compatibility between ARMAR and TRMM allows ARMAR to provide information useful for the TRMM radar design, for rain retrieval algorithm development, and for postlaunch calibration. ARMAR has additional capabilities, including multiple polarization, Doppler velocity measurement, and a radiometer channel for brightness temperature measurement. The system has been tested in both ground-based and airborne configurations. This paper describes the design of the system and shows results of field tests.

1. Introduction

A key factor in our understanding of the global water and energy cycle is the accurate measurement of rainfall. As a step toward achieving this goal, the Tropical Rainfall Measuring Mission (TRMM) will be launched in the late 1990s and will carry as one of its instruments a single-frequency, cross-track scanning radar for precipitation measurement (Simpson et al. 1988). The TRMM radar will be the first spaceborne radar for rainfall measurement. Rainfall measurement by ground-based radars remains a challenging problem, primarily because of the variability in the drop size distribution in space and time (Wilson and Brandes 1979; Austin 1987). Rainfall measurement by spaceborne radar faces these same challenges and is complicated by downward-looking geometry and by use of higher, attenuating frequencies because of antenna size constraints. To gain a better understanding of these issues before the launch of TRMM, the National Aeronautics and Space Administration (NASA) and the Jet Propulsion Laboratory (JPL) have developed an airborne rain-mapping radar (ARMAR) that flies on the NASA DC-8 aircraft and operates with the TRMM radar frequency and geometry. This paper describes ARMAR and shows results from field tests. Representative results are shown to illustrate the performance of the system. Detailed scientific analyses using data from ARMAR will be presented in future publications.

Corresponding author address: Dr. Stephen Durden, Jet Propulsion Laboratory, California Institute of Technology, 4800 Oak Grove Drive, Pasadena, CA 91109-8099.

2. Design considerations

Table 1 lists characteristics of the TRMM radar. Details concerning the TRMM radar design can be found in Awaka et al. (1988), Meneghini and Kozu (1990), and Nakamura et al. (1990). The 13.8-GHz frequency was selected as a compromise between antenna size and attenuation. At frequencies substantially below 13.8 GHz, the antenna size needed for a reasonable spatial resolution is too large for a spaceborne system. At frequencies substantially above 13.8 GHz, the attenuation in heavy rain would render it difficult to measure rainfall near the surface. The cross-track scanning geometry was chosen because it provides better vertical resolution than conical scanning. A conically scanned antenna is always pointed at a nonnadir angle, causing the resolution volume to be tilted and degrading the vertical resolution.

The primary design goal for ARMAR was to develop a system that matches the TRMM radar in both frequency and scanning geometry. ARMAR therefore operates at 13.8 GHz and has the cross-track scanning geometry of Fig. 1. This basic compatibility between ARMAR and TRMM allows ARMAR to provide information useful for the TRMM radar design, for rain

TABLE 1. TRMM radar system parameters.

Frequency	13.8 GHz
Altitude	350 km
Scanning swath	220 km
Surface horizontal resolution	4 km
Range resolution	250 m
Pulse duration	1.7 μs
Peak power	600 W

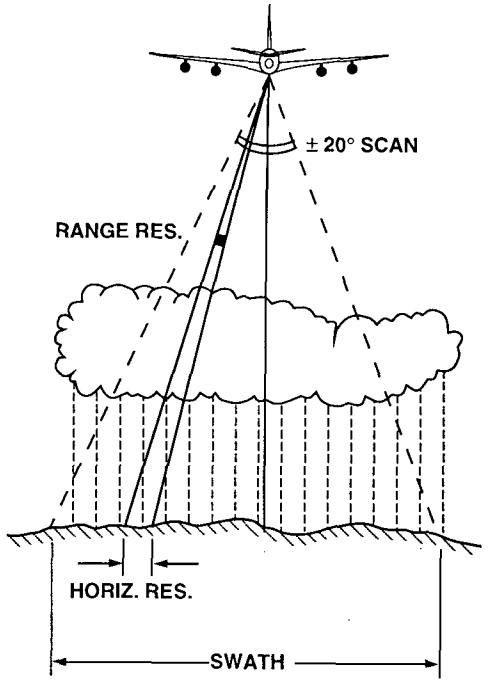

FIG. 1. ARMAR observational geometry.

TABLE 2. ARMAR system parameters.

Performance characteristics	
Range resolution (6-dB width)	80 m
Surface horizontal resolution (12-km altitude)	800 m
Swath width	9 km
Frequency	13.8 GHz
Polarizations	HH, VV, HV, VH
Antenna characteristics	
Aperture diameter	0.4 m
Gain	34 dB
3-dB beamwidth	3.8°
Sidelobe level	−32 dB
Polarization isolation	−28 dB
Transmitter characteristics	
Peak power	200 W
PRF	1–8 kHz
Number of transmit frequencies	1–4
Pulse duration	5–45 μs
Chirp bandwidth	4 MHz
Receiver characteristics	
System noise temperature	650 K
Sample frequency	10 MHz
ADC resolution	12 bit
Radiometer characteristics	
Bandwidth	40 MHz
ΔT per pixel	1 K

retrieval algorithm development, and for postlaunch calibration. A number of capabilities have been included on ARMAR that improve its ability to support the TRMM radar and will allow it to serve as a test bed for future spaceborne systems. For example, ARMAR has been designed to have finer spatial resolution than TRMM, so that issues such as the effect of partial beam filling can be studied. ARMAR can make like-polarization, cross-polarization, or alternating dual-polarization measurements. ARMAR can obtain a greater number of independent samples than the TRMM radar by using frequency diversity, transmitting up to four slightly different frequencies. When using a single transmit frequency, ARMAR is coherent, providing Doppler information. For situations in which a high accuracy in Doppler measurement is necessary, the antenna can be pointed at nadir rather than scanned, allowing a substantially larger dwell time and improved Doppler resolution. While operating as a radar, a small fraction of time is spent measuring brightness temperature in a radiometer mode at the same frequency and viewing geometry as the radar mode. Finally, ARMAR uses pulse compression (Cook and Bernfield 1967) to achieve the required range resolution. For a given peak transmit power and range resolution, pulse compression radars have a substantially higher signal-to-noise ratio (SNR) than conventional short-pulse systems. This would be useful for spaceborne radars, where peak power is limited. ARMAR's performance characteristics are summarized in Table 2. Figure 2 shows the expected single-pulse SNR for a uniform rain column with different rain rates, using a 5-μs transmitted pulse and radar altitude of 10 km. Longer pulses provide proportionately higher SNRs.

As mentioned in the introduction, one of the challenges faced by spaceborne radars is the downward-looking geometry. This creates the possibility of surface

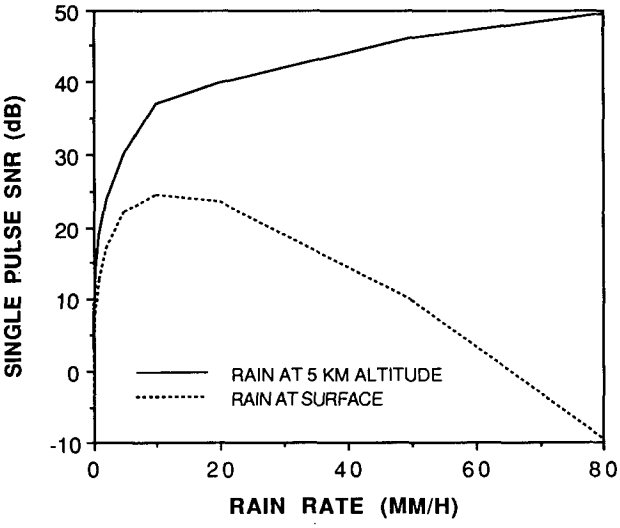

FIG. 2. Theoretical single-pulse signal-to-noise ratio as a function of rain rate for a 5-km column of uniform rain. The radar is at an altitude of 10 km.

clutter, that is, return from the surface obscuring return from precipitation. In the case of a downward-looking 13.8-GHz radar, return from the surface can be 35–55 dB greater than return from 0.5 mm h^{-1} rain, depending on the ocean cross section and the radar range resolution (Okamoto et al. 1988; Hanado and Ihara 1992). For an antenna that is looking off-nadir, it is possible for the surface at nadir to be at the same range as precipitation. For the antenna mainlobe return from precipitation to be detectable above the surface sidelobe return, the sidelobes in the two-way antenna pattern relative to the mainlobe must be near −60 dB. This corresponds to −30 dB sidelobes in the one-way pattern. Also of concern are pulse compression sidelobes. Because they extend over many range bins, it is possible for sidelobes associated with the surface return to obscure return from rain. As in the antenna case, the pulse compression sidelobes should be near −60 dB relative to the peak return. These requirements are discussed further in Li et al. (1987), Manabe and Ihara (1988), Meneghini and Kozu (1990), and Nakamura et al. (1990).

We performed computer simulations of a variety of pulse compression sidelobe suppression techniques (Cook and Bernfield 1967) and found that a linear upsweep frequency modulated chirp with time domain amplitude weighting could achieve the required sidelobe performance. Time domain weighting has not been widely used because the final, high power amplifier in most radars operates in saturation. We chose to use this technique and operate the high-power amplifier in the linear rather than saturated region. In specifying the shape of the transmitted chirp, we were faced with a trade-off between range sidelobe levels, resolution, and SNR. Optimal SNR and range resolution are achieved by a constant amplitude pulse. Optimal sidelobe performance is achieved, however, by using a smooth envelope over the entire transmitted chirp. Based on computer simulations, we decided to use a raised half-wave sinusoidal function that varies from zero at the start of the chirp to one during the first third of the chirp. The middle third of the chirp has constant amplitude of 1, and the final third of the chirp is again multiplied by a raised half-wave sinusoid to vary smoothly from 1 to 0. In using this amplitude weighting, there is a loss of approximately 2 dB in SNR over a uniform amplitude and a broadening of the 3-dB range resolution from 35 to 55 m. However, the theoretical pulse compression sidelobe performance of this weighting is better than −60 dB, as required.

3. System description

A simplified block diagram of ARMAR is shown in Fig. 3. The digital controller causes the chirp generator to produce chirps with the selected length, spacing, and start frequency. The chirp amplitude and frequency dependence are stored in a look-up table in the digital controller and can be changed in software, allowing waveforms with arbitrary amplitude and frequency dependence to be generated. In normal operation, the waveform is a linear frequency modulated upsweep chirp with 4-MHz bandwidth and amplitude weighting as described in the previous section. Details of the circuitry used to generate the chirp can be found in Tanner et al. (1994). The chirp start frequencies range from 55 to 81 MHz, and up to four different start frequencies can be used in sequence, quadrupling the number of independent samples at a given pulse repetition frequency (PRF). For Doppler measurements the system must be coherent, so only a single frequency is used. The chirps are upconverted to 13.8 GHz and amplified by a high-power traveling-wave tube amplifier (TWTA). The amplified chirp is then sent to the antenna system. A small amount of power is sent directly to the receiver through a calibration loop with 84.5-dB attenuation. The TWTA is operated in the nonsaturated mode to maintain the desired chirp amplitude characteristics.

The antenna system consists of a dual, linearly polarized scalar feedhorn that illuminates a precision offset parabolic reflector. The signal is focused by the parabolic reflector and reflected to a flat mechanically scanned elliptical reflector that scans the beam ±20° in the cross-track direction. The reflector can also be pointed or scanned up to ±10° in the along-track direction, if desired. The offset antenna design was chosen because of its low sidelobes, −32 dB, required for minimizing surface clutter. Both transmit and receive polarizations can be varied on a pulse to pulse basis, allowing a combination of like- and/or cross-polarization data to be collected. The signal reflected from the rain is collected by the antenna and then amplified by a low-noise amplifier (LNA). Following the LNA, the received signal is downconverted to the 70-MHz intermediate frequency (IF). Here, the signal is split into radar and radiometer signals. The radar signal is passed through a programmable attenuator before IF amplifiers and filters. In the final stage, the signal is downconverted to baseband (offset video) where it is digitized by a 12-bit analog–digital converter (ADC) at a rate of 10 MHz and recorded. The IF programmable attenuator is normally set so that less than 1% of the received pulses cause the ADC to overflow. The baseband signal is also sent to an oscilloscope for a real-time A-scope display of the data. The radiometer signal is acquired during a short time within each interpulse period after return from the transmitted pulse has reached zero. This signal is integrated in analog circuitry, sampled every 10 ms, averaged, and recorded. At the end of each scan (or every few seconds in nadir-looking operation), ARMAR records several hundred calibration loop chirps and radiometer measurements of the transmit–receive switch reference load and a temperature-controlled noise diode. These measure-

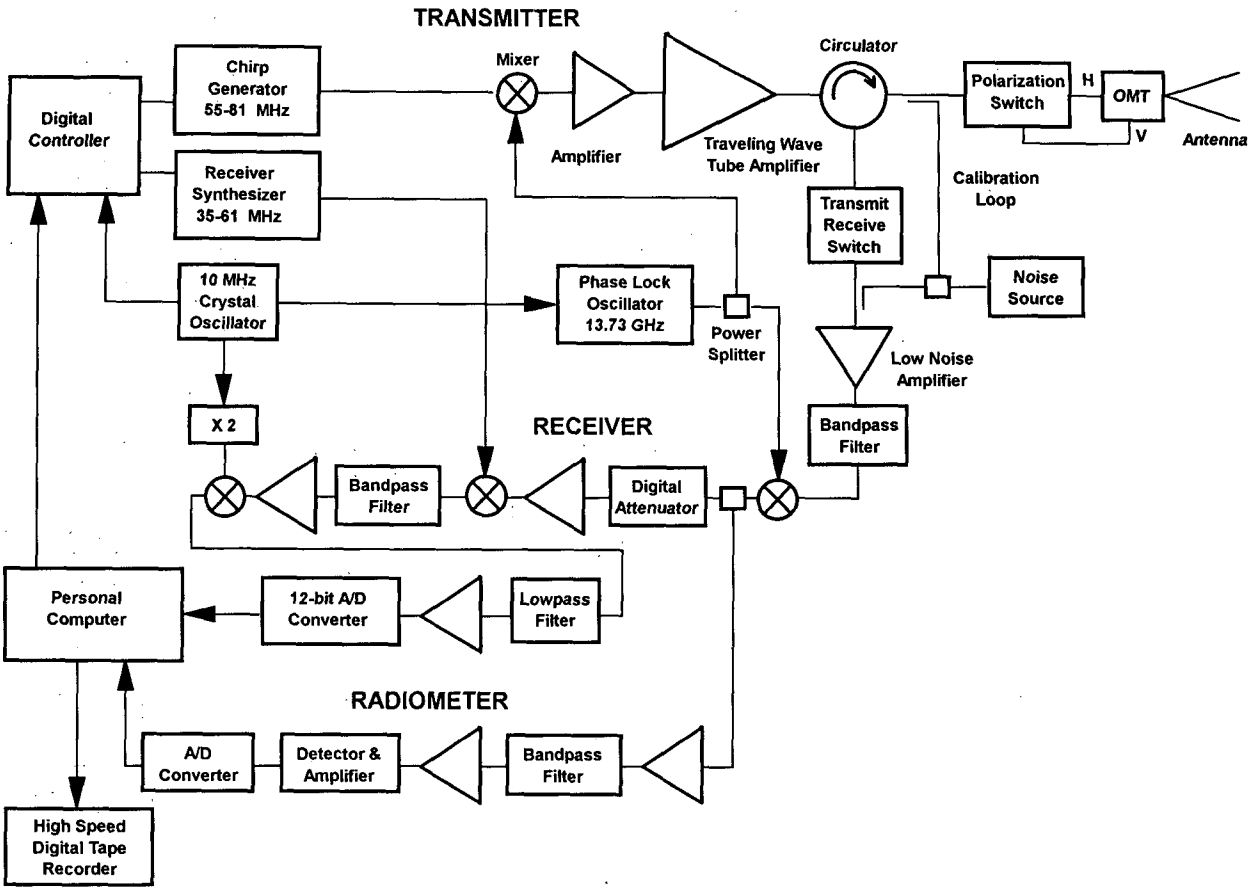

FIG. 3. Block diagram of ARMAR transmitter and receiver.

ments are used by the data processing system for calibration.

A diagram of the control and data handling is shown in Fig. 4. The main control computer is a 486 personal computer (PC). This computer runs a Quick Basic program for overall system control. A VME 68000 computer is used for real-time control of the radar through a specially designed digital controller. The VME computer also controls the antenna scanner. The signal conditioner and formatter board in the PC receives the data from the 12-bit ADC and transmits it to a high-speed Ampex DCRSi tape recorder. Radiometer and auxiliary data, including system temperatures and aircraft parameters from the DC-8 data system, are recorded along with the radar data. There is also a Zoran FFT (fast Fourier transform) processor board in the PC that is used for pulse compression of selected pulse for a real-time display. During operation, it is possible to display the radar configuration or samples of the received uncompressed and compressed pulse along with engineering data.

The data processing system consists of a Sun workstation and a Sky Computers i860-based coprocessor. This system correlates the recorded data with a model of the transmitted signal to perform pulse compression. The average magnitude squared is calculated and converted to the ratio of received to transmitted powers using calibration chirp data and laboratory measurements of the transmit path, receive path, and calibration loop attenuations. This ratio, along with the range, range resolution, and antenna pattern are used in the radar equation to calculate the equivalent reflectivity factor Z_{eq}. For Doppler mode data, the complex compressed signal is used in a pulse-pair algorithm (Doviak and Zrnić 1984) to estimate the mean velocity and spectrum width. For dual-polarization modes, appropriate polarimetric quantities are calculated, in addition to reflectivity and velocity. Radiometer voltages are converted to brightness temperatures using the noise diode and reference load measurements. The processed data can be displayed on the Sun workstation under X Windows.

The radar system is mounted in the cargo bay of the NASA DC-8 aircraft. The antenna beam is directed through an opening in the bottom of the DC-8 aircraft. A thin radome covers this observation port, and the entire antenna system is surrounded by a pressure box. The radar radio frequency (RF) section is mounted

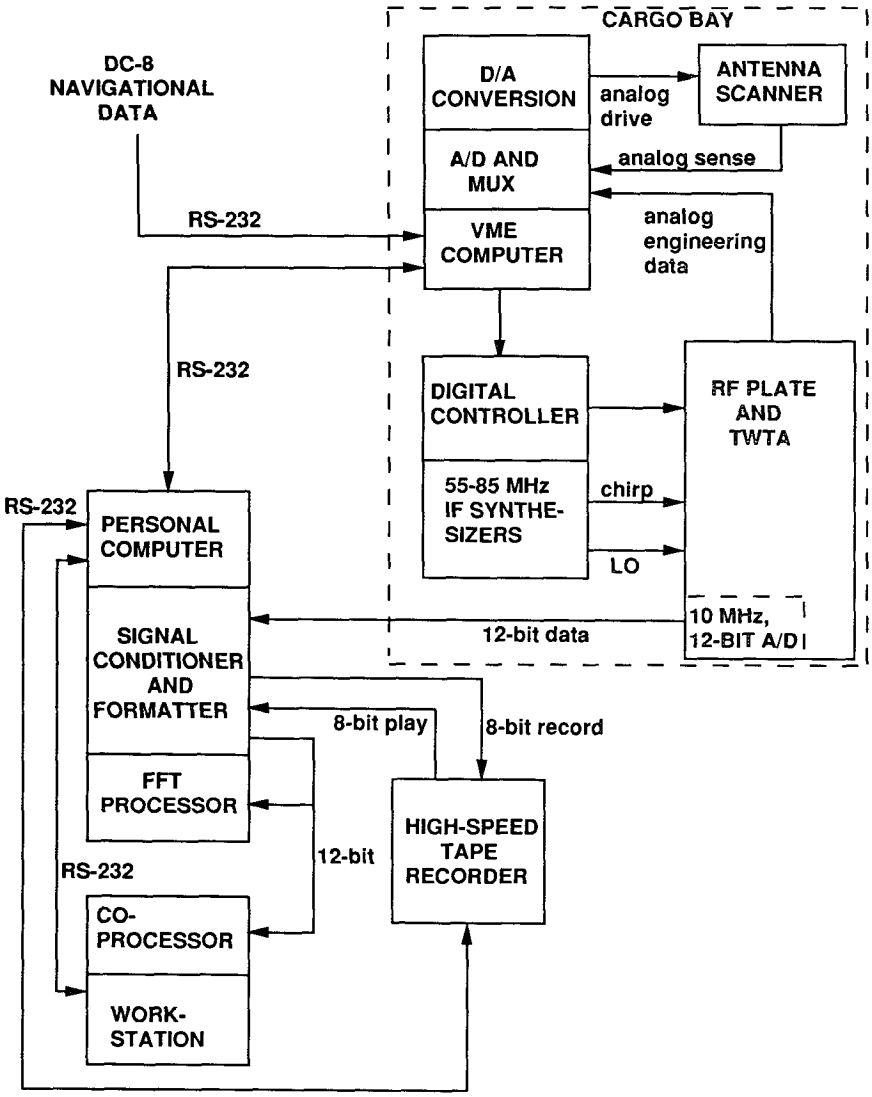

FIG. 4. Diagram showing ARMAR control and data handling.

on a plate that lays on top of the pressure box. This plate also includes IF, video, and ADC sections; a photograph of it is shown in Fig. 5. A rack for the TWTA and other equipment is mounted in the cargo bay next to the pressure box. The system computer, tape recorder, and data processing system are mounted in a rack in the DC-8 cabin where the ARMAR operators sit.

4. Field tests

a. System parameter measurements

ARMAR was field tested in a ground-based configuration during several occasions in 1991–92 and was flight tested on the NASA DC-8 aircraft in May and December of 1992. The primary goal of these tests was to verify that the radar meets design specifications. Data were acquired under both clear and raining conditions, allowing the following system parameters to be measured: 1) pulse compression sidelobes, 2) antenna sidelobes, 3) antenna cross-polarization isolation, 4) noise level, 5) system coherence, and 6) calibration accuracy. This section consists of a description of system parameter measurements, followed by examples of rainfall measurements.

As discussed previously, pulse compression sidelobes must be near -60 dB for the radar to measure 0.5 mm h^{-1} rainfall over the ocean. To verify the pulse compression sidelobes, data were acquired for chirp lengths ranging from 5 to 45 μs while flying over the ocean under clear conditions. The data were processed and averaged over several thousand pulses; results for the 20-μs case are shown in Fig. 6. The pulse compres-

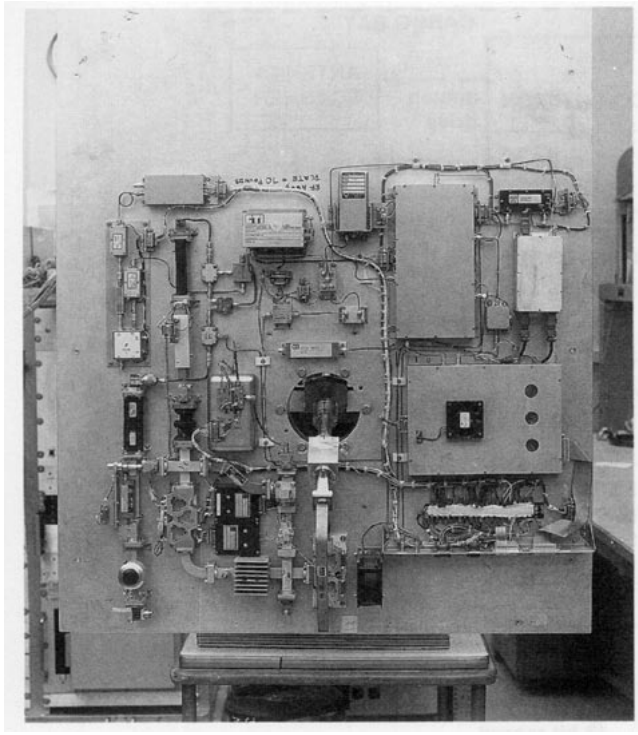

FIG. 5. Photograph of the ARMAR RF plate.

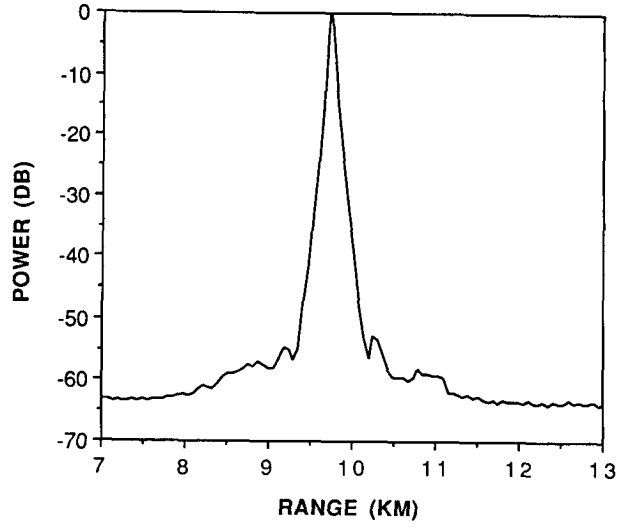

FIG. 6. Average of approximately 6000 compressed pulses from airborne measurements of the ocean surface using a 20-μs chirp.

sion sidelobes are in the −55- to −60-dB range, demonstrating that the system can measure relatively light rainfall over the ocean. The results shown here are typical of the system's operation.

As stated in section 2, the antenna sidelobes must be −30 dB or lower because of signal to surface clutter considerations. Antenna range measurements indicated a sidelobe level of −32 dB. To verify the antenna sidelobe performance with the antenna on the aircraft, two airborne experiments were performed. In the first, the radar was flown over a ground-based, vertically pointing transmitter, which transmitted a continuous 13.80-GHz tone. ARMAR's transmitter was off; otherwise, the rest of the ARMAR system was operating normally. The tone from the ground-based transmitter was received by ARMAR's antenna, mixed down to 70 MHz in the IF stage, and then mixed with 68 MHz to get a 2-MHz tone in the video stage. While flying over the transmitter, the antenna was rapidly scanned so that several antenna scans were acquired while ARMAR was in the ground transmitter's antenna beam. The resulting dataset consists of segments of the transmitter signal sampled at 10 MHz, with each segment containing 1024 samples. The segments are spaced by the pulse repetition period, approximately 200 μs. Each 1024-point segment was Fourier transformed and the power at the transmitter frequency was extracted, giving a time series of received power. The cross-track antenna pattern was obtained from this time series during a scan when the aircraft was directly over the ground transmitter. The along-track pattern was obtained from the maximum return in each scan as the aircraft passed over the transmitter. The results are shown in Fig. 7. The antenna sidelobes are approximately −30 dB, which is similar to antenna range measurements made before installation of the system on the DC-8 aircraft.

The pattern shown in Fig. 7 is for the antenna near its nadir-looking position. To verify sidelobe performance at scan angles far from nadir, the aircraft was rolled to 30° to give a large incidence angle on the ocean surface and allow separation of mainlobe and sidelobe return in range. The antenna was scanned ±20°, giving incidence angles from 10° to 50°. Figure

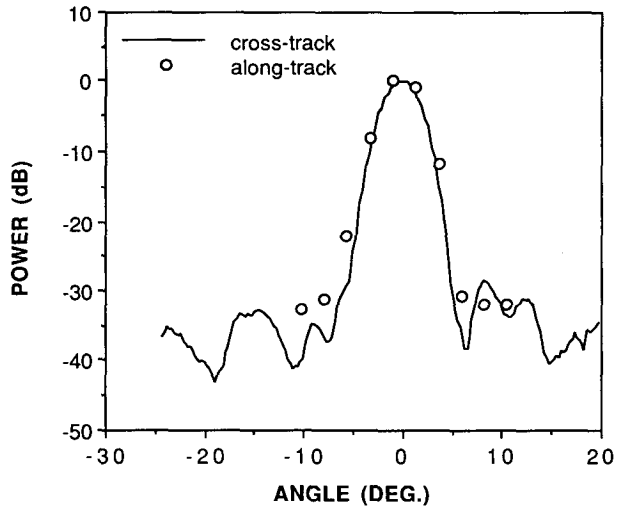

FIG. 7. Cross-track and along-track antenna patterns as measured by flight over a 13.8-GHz transmitter on the ground.

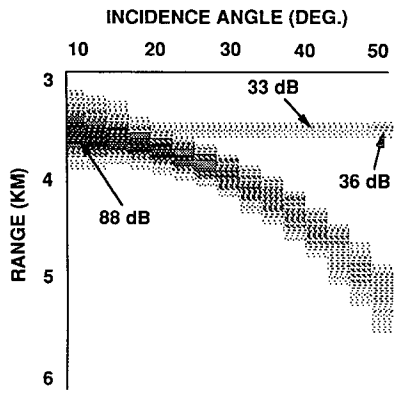

FIG. 8. Image showing measured power as a function of incidence angle (horizontal axis) and range (vertical axis). Maximum received power is shown in black; a 65-dB dynamic range is displayed.

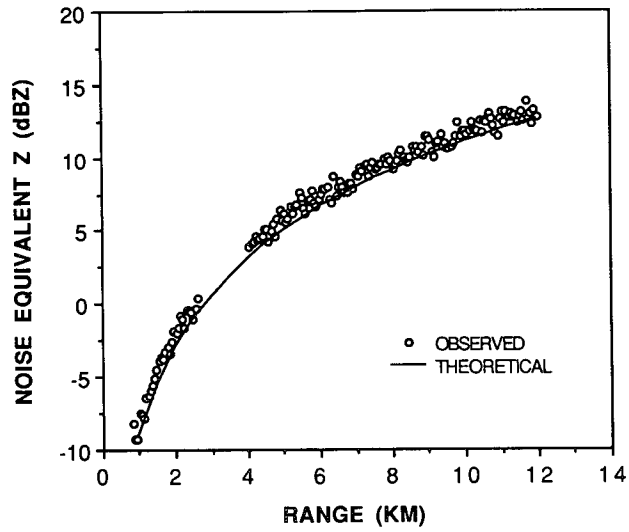

FIG. 9. Noise equivalent reflectivity factor as a function of range. This quantity is the minimum detectable Z_{eq} at a given range. Both observed and theoretical values are shown.

8 shows the received power as a function of range (vertical axis) and incidence angle (horizontal axis) for a roll to the left. The dynamic range displayed in this image is approximately 65 dB, with black showing the maximum return. The mainlobe return follows a curved pattern since the range to the ocean increases with incidence angle. The sidelobe return is always at the range corresponding to nadir (3.5 km) and is visible as a straight line that gets slightly darker near 50° incidence. The 3-dB increase in sidelobes at the maximum scan angle suggests that the antenna pattern degrades slightly, as the beam gets nearer to the edge of the observation port. The maximum sidelobe return (36 dB) is 52 dB less than the mainlobe return at 10° (88 dB). The mainlobe return at nadir (not shown) is typically 6–8 dB greater than at 10°, and is, therefore, approximately 60 dB greater than the maximum sidelobe return. Both left and right aircraft rolls were executed, and the sidelobe return was always less than or equal to approximately −60 dB relative to the nadir mainlobe return.

The cross-polarization isolation of the system is the level at which a like-polarized target is seen in the cross-polarized channel. Estimates of the antenna cross-polarization isolation can be determined from HH–HV dual-polarization measurements of the ocean surface. At nadir over the ocean the cross-polarized return is consistently 28 dB below the like-polarized return. Since the true cross-polarized ocean cross section at nadir is not known, this measurement provides a bound on the cross-polarization isolation. The actual system cross-polarization isolation is −28 dB or better.

To determine the system noise level, clear air data were used. By converting these noise measurements into the equivalent reflectivity factor Z_{eq}, the minimum observable reflectivity factor as a function of range was found. Figure 9 compares the observed noise equivalent reflectivity factor with the value calculated from theory using system parameters. Note that the surface return occurred at a range of approximately 3.5 km and has been removed from the observations. The observed system noise level is very close to the theoretical noise level.

The system coherence can be verified by examining the Doppler spectrum width. When the radar is airborne, the measured spectrum is broadened by the aircraft motion, just as the spectrum measured by ground-based systems is broadened by a tangential wind (Sloss and Atlas 1968). Figure 10 shows the measured spectrum for nadir-looking, airborne measurements of a land surface. Plotted on the same figure is the theoret-

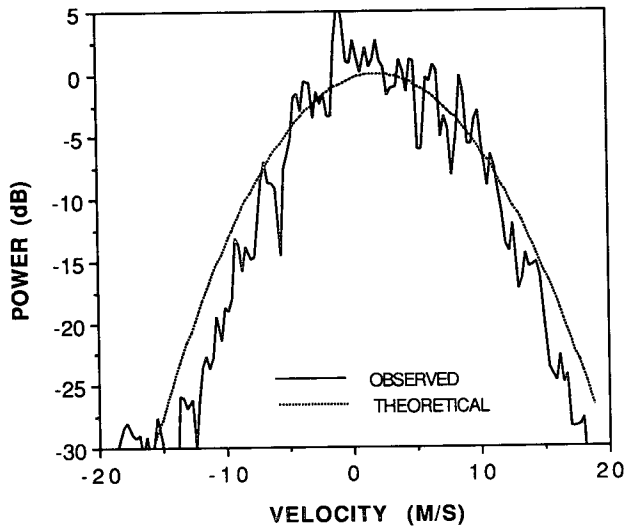

FIG. 10. Measured Doppler spectrum for airborne measurement of land surface. The theoretical spectrum derived from an antenna pattern model is shown for comparison.

ical spectrum based on a Gaussian approximation to ARMAR's antenna pattern and the assumption that the surface cross section is constant with incidence angle for incidence angles within 5° of nadir. A lack of coherence would cause the measured spectrum to be broader than the theoretical. In fact, the measured spectrum is slightly narrower than the theoretical, probably because the surface cross section decreases with increasing incidence angle.

The accuracy of the radar calibration was verified by examining return from the ocean for several flight days. These data were processed to produce estimates of the normalized radar cross section $\sigma°$, as a function of incidence angle (shown in Fig. 11). Measurements by ocean scatterometers have shown that $\sigma°$ at 10° is nearly independent of wind speed and is approximately 7 dB (Schroeder et al. 1985). ARMAR's measurements at 10° are within ±3 dB of this value. The relative calibration between polarization channels was checked by examining dual-polarization (HH–VV) data acquired over the ocean at nadir incidence. For this case HH and VV should be identical; the measured HH and VV differed by only 0.05 dB.

b. *Rainfall observations*

In this section ground-based and airborne observations of rainfall are presented. Figure 12 shows ground-based, vertically pointing measurements of rainfall at JPL on 6 February 1992. The rain was stratiform, and a well-defined bright band can be seen in the reflectivity plot at a range (altitude) of approximately 2 km. The velocity plot shows large increases in the fall velocity just below the bright band. The increase in velocity is expected as the ice particles completely melt and shrink

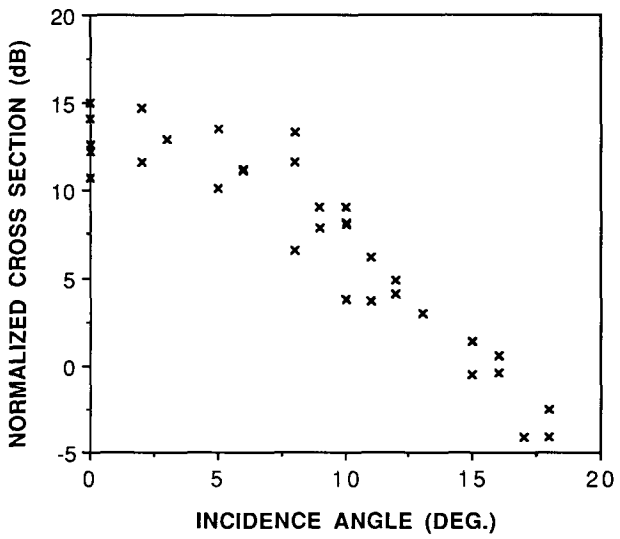

FIG. 11. Airborne measurements of ocean backscatter cross section $\sigma°$ as a function of incidence angle.

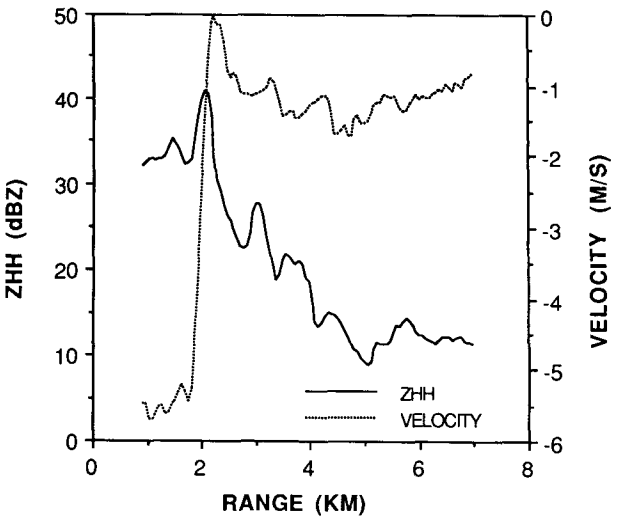

FIG. 12. Data acquired in ground-based, vertically pointing configuration at JPL, 6 February 1992, plotted vs range from radar. Negative velocity is toward radar (downward).

in size. Rainfall was measured with a tipping-bucket raingage located close to the radar. Rain rates were calculated from the accumulated rainfall as a function of time, and the rain rate corresponding to the radar data in Fig. 12 was 5 mm h^{-1}. The measured reflectivity and velocity are consistent with a 5 mm h^{-1} rain rate (Atlas et al. 1973). Data were also acquired in a horizontally pointing configuration (15° elevation angle) using the HH–VV dual-polarization mode. Figure 13 shows the HH reflectivity Z_{HH}, the differential reflectivity Z_{DR}, and the two-way differential phase (Seliga and Bringi 1978), computed from 500 pulses. Each of these parameters shows a feature at a range of approximately 7 km, which is likely the melting layer (height of 2 km). The values of all three parameters are reasonable for light rain.

Figure 14 shows a cross-track reflectivity scan from a thunderstorm over Arizona on 7 May 1992. The surface is the dark line extending horizontally through the scan. Strong return from rainfall is visible above the surface at the left of the scan. This return is measured to be 48 dBZ, and is probably somewhat higher since ARMAR data is not currently corrected for attenuation. To the right of nadir some return seems to be coming from below the surface. This is mirror image return, where the radar signal reflects from the surface, from rain, and from surface again (Atlas and Matejka 1985). The brightness temperature for this area was approximately 40 K cooler than the surrounding areas, suggesting a highly reflective surface. The Doppler velocity for this area indicated motion toward the radar, consistent with mirror image scattering. Although a topographic map did not show any large bodies of water in this area, it did show a mesa and several creek beds. Rainfall may have increased the surface reflectivity,

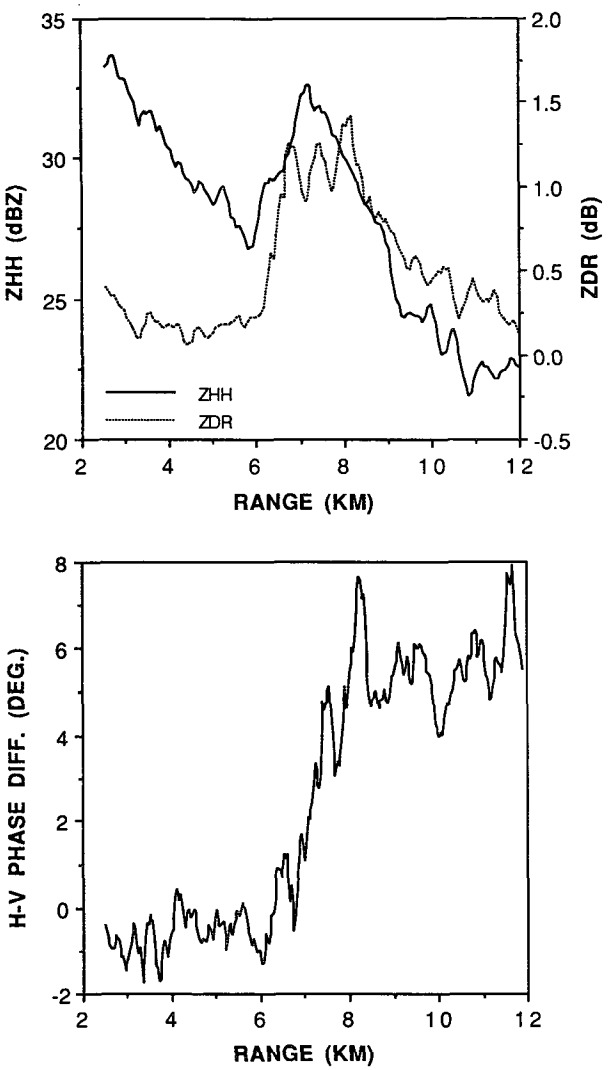

FIG. 13. Data acquired in ground-based, horizontally pointing configuration at JPL, 6 February 1992, using HH–VV dual polarization. (upper) The HH polarization reflectivity and differential reflectivity. (lower) Two-way HH–VV phase difference.

causing the mirror image return. Figure 15 shows plots of the nadir data from this scan. The reflectivity steadily increases downward until a maximum of 42 dBZ is reached at 2 km above the surface. Beyond this the reflectivity decreases, possibly because of evaporation in the desert environment. The surface return has two distinct peaks separated by a little less than 100 m, due to surface topography. This is consistent with the topographic map, which showed hills surrounding the mesa mentioned previously. Even with topography there appears to be weak mirror image return beyond the surface return. The velocity also indicates this, becoming negative (toward radar) for range bins beyond the surface. National Weather Service radar classified the rainfall from this storm as moderate, in agreement with our measured return.

Figure 16 shows a cross-track reflectivity scan from a stratiform rain area over the equatorial Pacific, 21 May 1992, and Fig. 17 shows nadir data from this scan. A bright band is evident in the reflectivity data at an altitude of about 4.7 km, and a jump in velocity occurs at the bright band. In contrast with Fig. 15, the surface return in Fig. 17 is narrow and symmetric because of the flatness of the ocean. Strong mirror image return is evident in Figs. 16 and 17, as would be expected over the ocean. The measured velocities are 1–2 m s^{-1} higher than predicted by theoretical calculations of v versus Z (Atlas et al. 1973). The measured brightness temperature in this case was 220 K, which is consistent with moderate rainfall over the ocean (Fujita et al. 1985).

5. Summary

A 13.8-GHz airborne rain-mapping radar (ARMAR) has been developed by NASA/JPL. ARMAR was designed as a prototype for spaceborne rain radars, and its frequency and scanning geometry are identical to the TRMM radar. It has a spatial resolution cell size that is smaller than that of the TRMM radar. It also has Doppler and multiple polarization capabilities and

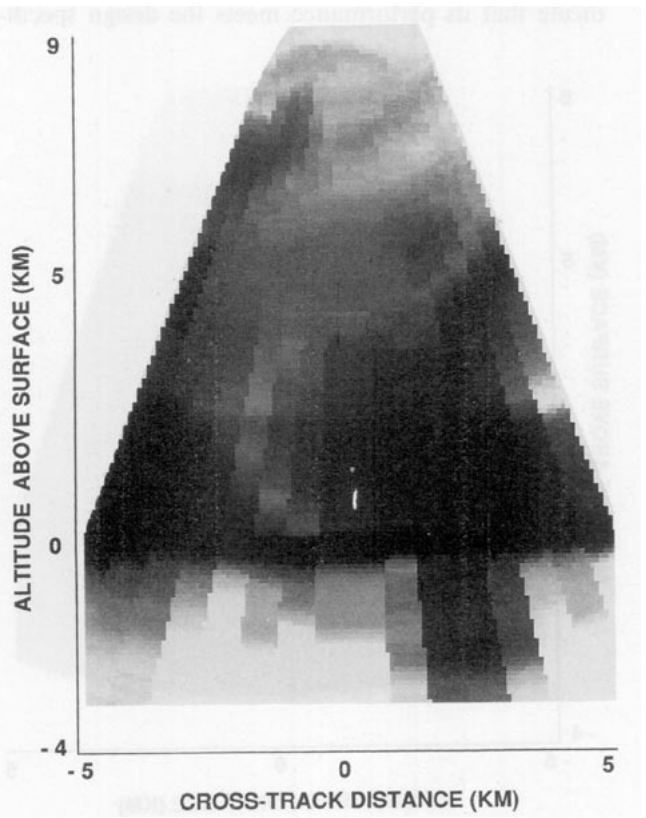

FIG. 14. Cross-track scan from airborne observation of the Arizona thunderstorm of 7 May 1992. Reflectivity varies from 10 dBZ (white) up to 50 dBZ (black). Aircraft altitude is 12 km. Ground swath width is 8.6 km.

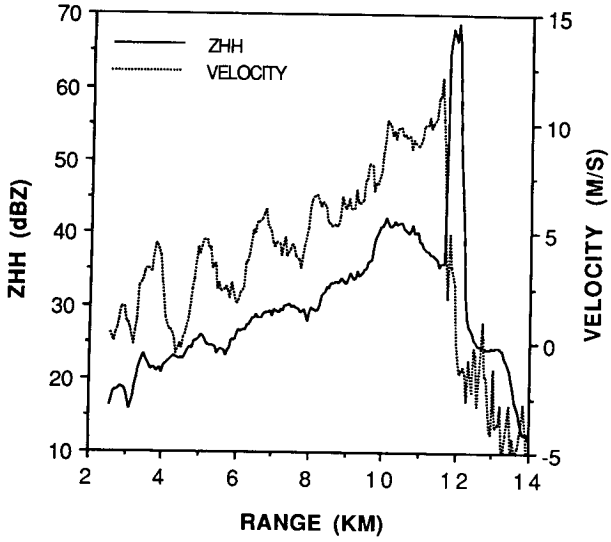

FIG. 15. Nadir-looking data from the scan of Fig. 14 over an Arizona thunderstorm, plotted vs range from radar. Positive velocity is away from radar (downward).

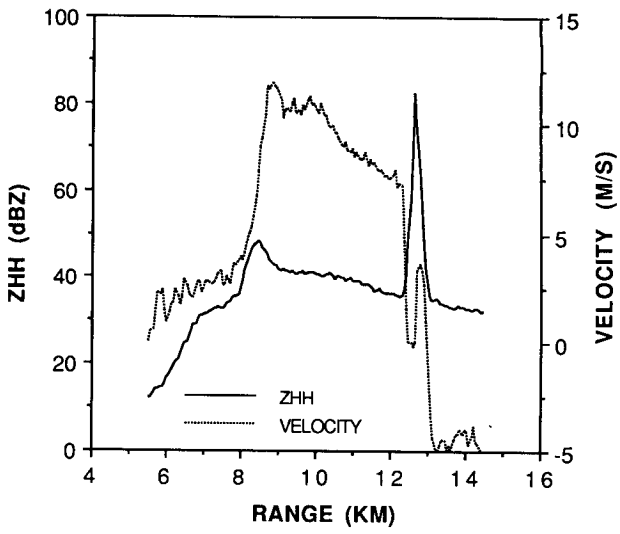

FIG. 17. Nadir-looking data from the scan of Fig. 16 over a Pacific rainstorm, plotted vs range from radar. Positive velocity is away from radar (downward).

measures the 13.8-GHz brightness temperature. Ground-based and airborne field tests of ARMAR indicate that its performance meets the design specifications. ARMAR is now an operational instrument, and the first operational measurements using ARMAR occurred in the TOGA COARE experiment in January and February 1993. The instrument worked well and analyses of the data have begun. Further experiments in support of the TRMM radar system and rain retrieval algorithm development will be carried out in the future.

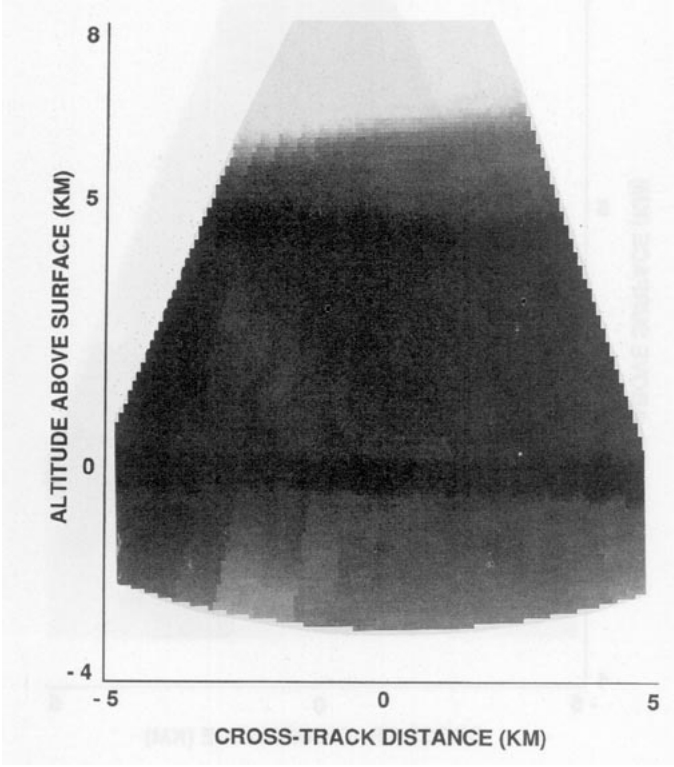

FIG. 16. Cross-track scan from airborne observation of a rainstorm in the equatorial Pacific Ocean on 21 May 1992. Reflectivity varies from 10 dBZ (white) up to 50 dBZ (black). Aircraft altitude is 12.6 km. Ground swath width is 9.2 km.

Acknowledgments. The research described here was performed by the Jet Propulsion Laboratory, California Institute of Technology, under contract with NASA.

REFERENCES

Atlas, D., and T. Matejka, 1985: Airborne Doppler radar velocity measurements of precipitation seen in ocean surface reflection. *J. Geophys. Res.*, **90,** 5820–5828.

——, R. C. Srivastava, and R. S. Sekhon, 1973: Doppler radar characteristics of precipitation at vertical incidence. *Rev. Geophys. Space Phys.*, **11,** 1–35.

Austin, P., 1987: Relation between measured radar reflectivity and surface rainfall. *Mon. Wea. Rev.*, **115,** 1053–1070.

Awaka, J., T. Kozu, and K. Okamoto, 1988: A feasibility study of rain radar for the tropical rainfall measuring mission, 2. Determination of basic system parameters. *J. Comm. Res. Lab.*, **35,** 111–133.

Cook, C. E., and M. Bernfield, 1967: *Radar Signals: An Introduction to Theory and Application.* Academic Press, 531 pp.

Doviak, R. J., and D. S. Zrnić, 1984: *Doppler Radar and Weather Observations.* Academic Press, 103–107.

Fujita, M., K. Okamoto, H. Masuko, T. Ojima, and N. Fugono, 1985: Quantitative measurements of path-integrated rain rate by an airborne microwave radiometer over the ocean. *J. Atmos. Oceanic Technol.*, **2,** 285–292.

Hanado, H., and T. Ihara, 1992: Evaluation of surface clutter for the design of the TRMM spaceborne radar. *IEEE Trans. Geosci. Remote Sens.*, **30,** 444–453.

Li, F. K., K. E. Im, W. J. Wilson, and C. Elachi, 1987: On the design issues for a spaceborne rain mapping radar. *Tropical Rainfall*

Measurements, J. Theon and N. Fugono, Eds., A. Deepak Publishing, 387–393.

Manabe, T., and T. Ihara, 1988: A feasibility study of rain radar for the tropical rainfall measuring mission, 5. Effects of surface clutter on rain measurements from satellite. *J. Comm. Res. Lab.,* **35,** 163–181.

Meneghini, R., and T. Kozu, 1990: *Spaceborne Weather Radar.* Artech House, 199 pp.

Nakamura, K., K. Okamoto, T. Ihara, J. Awaka, T. Kozu, and T. Manabe, 1990: Conceptual design of rain radar for the tropical rainfall measuring mission. *Int. J. Satellite Comm.,* **8,** 257–268.

Okamoto, K., J. Awaka, and T. Kozu, 1988: A feasibility study of rain radar for the tropical rainfall measuring mission: 6. A case study of rain radar system. *J. Comm. Research Lab.,* **35,** 183–208.

Schroeder, L. C., P. R. Schaffner, J. L. Mitchell, and W. L. Jones, 1985: AAFE RADSCAT 13.9 GHz measurements and analysis: Wind-speed signature of the ocean. *IEEE J. Oceanic Eng.,* **10,** 346–357.

Seliga, T. A., and V. N. Bringi, 1978: Differential reflectivity and differential phase shift: Applications in radar meteorology. *Radio Sci.,* **13,** 271–275.

Simpson, J., R. F. Adler, and G. R. North, 1988: A proposed Tropical Rainfall Measuring Mission (TRMM) satellite. *Bull. Amer. Meteor. Soc.,* **69,** 278–295.

Sloss, P. W., and D. Atlas, 1968: Windshear and reflectivity gradient effects on Doppler radar spectra. *J. Atmos. Sci.,* **25,** 1080–1089.

Tanner, A., S. L. Durden, R. Denning, E. Im, F. K. Li, W. Ricketts, and W. Wilson, 1994: Pulse compression with very low sidelobes in an airborne rain mapping radar. *IEEE Trans. Geosci. Remote Sensing,* in press.

Wilson, J. W., and E. A. Brandes, 1979: Radar measurements of rainfall. *Bull. Amer. Meteor. Soc.,* **60,** 1048–1058.